



Final Draft **of the original manuscript**

Jeong, Y.; Steglich, D.:

Modelling-assisted description of anisotropic edge failure in magnesium sheet alloy under mixed-mode loading.

In: International Journal of Mechanical Sciences. Vol. 181 (2020) 105680.

First published online by Elsevier: 20.05.2020

<https://dx.doi.org/10.1016/j.ijmecsci.2020.105680>

Modelling-assisted description of anisotropic edge failure in magnesium sheet alloy under mixed-mode loading

Youngung Jeong^{1,*} and Dirk Steglich²

¹Department of Materials Science and Engineering, Changwon National University, 20 Changwondaehak-ro, Changwon, 51140 Gyeongnam, Republic of Korea

²Institute of Materials Research, Materials Mechanics, Helmholtz-Zentrum Geesthacht, Max-Planck-Str. 1, 21502 Geesthacht, Germany

*Corresponding author email: yjeong@changwon.ac.kr

Abstract

An uncoupled fracture criterion based on a simple damage indicator computed using a mean-field crystal plasticity framework is proposed and applied to predict failure of an AZ31 sheet originating from the edges. The damage indicator quantifies the contribution of strain components along the axes of orthotropy leading to material failure. The model is calibrated by uniaxial tension tests. The damage indicator is validated for various mixed-mode deformation histories realized by modified Arcan tests in various loading configurations. The loading history of respective fracture sites obtained from DIC analyses is directly employed to a visco-plastic self-consistent crystal plasticity model to obtain the stress responses. The results indicate that the damage indicator requires – beside the strain history – an input of stress triaxiality, by which an improved predictive accuracy can be achieved. This effect is quantified for various loading scenarios, in which cracks are initiated near or at the edge of the sample.

1 Introduction

The application of magnesium alloy sheets in transportation industry demands for reliable simulation tools for predicting the forming capabilities, the structural responses to mechanical loads, and the lifetime of the components. The predictive models have to match the distinctive mechanical characteristics attributed to the low-symmetric hexagonal close-packed metal, which demands for state-of-the-art material laws. The selection of an appropriate yield function capturing plastic yielding under multi-axial stress states challenges many researchers. The prediction of damage events and material failure is a research topic on its own.

In the recent literature, various types of failure criteria are proposed, discussed and used for sheet metals. Generally, they can be categorized into three groups:

- Group I. Criteria focusing on plastic instabilities caused by strain-localization such as Hill [1], Swift [2] and Marciniak-Kuczyński [3,4];
- Group II. Coupled fracture criteria based on porous metal plasticity theory [5–7] that implicitly account for the presence and growth of voids, cavities and microcracks;
- Group III. Uncoupled fracture criteria using a damage indicator together with a non-porous plasticity theory [8–11].

Criteria of all three groups aim on predicting the location and time or state of material failure. Failure criteria are linked to the constitutive behavior of materials, since they use field quantities like stress and strain measures. In the case plastic deformation is considered, a plastic potential together with a flow rule and a strain-hardening concept implicitly link strains and stresses. Due to the significant role of stress measures in criteria addressing ductile failure (large amount of irreversible deformation precedes fracture) [12,13], the stress-associated model parameters depend on the chosen plasticity model. The plasticity model may provide the stress responses as an explicit function of strain, so that the failure criterion can be expressed as a function of strain only – see for example [14]. Typical for criteria of Group III is that it can be applied in a post-processing step after solving the boundary value problem, which reduces computational efforts compared to Group II approaches.

The use of phenomenological plasticity models with yield function and empirical strain-hardening rule prevails in various Group III fracture criteria. Detailed features and assumptions made on the phenomenological plasticity models vary depending on the material characteristics. For example, anisotropic yield functions are preferably assumed for materials with strong anisotropy, whereas isotropic yield functions are regarded more appropriate for materials without strong anisotropy due to their simplicity.

However, the conventional phenomenological plasticity models based on the isotropic hardening law face challenges when applied to magnesium alloys owing to two distinctive characteristics: 1) the magnesium alloys are in the low-symmetric hexagonal close-packed structure thus requiring deformation twinning in addition to slip modes to accommodate arbitrary deformation; and 2) magnesium sheets usually exhibit strong initial crystallographic texture, which may drastically evolve due to twinning depending on the loading condition. These two mentioned characteristics may lead to a pronounced strength differential (SD) effect [15–17]. It is well known that isotropic hardening laws cannot capture the SD effect, and deformation-induced anisotropy (due to crystallographic texture evolution) further complicates the description of the material behavior [18–23].

Progresses have been made by formulating the phenomenological yield criterion as an odd function of the stress deviator in order to capture the SD effect. The family of yield functions proposed by Cazacu, Plunkett and Barlat (hereinafter denoted as CPB) has been widely applied for various magnesium alloys in the literature [24,25]. The calibration and verification of the CPB yield function, however, often relies on the crystal plasticity framework [25,26], mainly due to the experimental difficulties to determine the model parameters under multiaxial loading conditions. Nevertheless, recent applications of the CPB yield function for Group III fracture criteria have been reported in the literature. For example, Jia and Bai [14,27] used the CPB06ex2 yield criterion [28] for AZ31B-H24 magnesium alloy. However, they did not include the variation of coefficients resulting from texture evolution due to twinning induced reorientation as suggested in [26]. They also utilized the semi-analytical Sachs model of Barnett et al. [29] in order to capture the SD effect. Furthermore, a linear transformation on the strain tensor was introduced to account for the fracture anisotropy similar to the way presented in [30,31] for aluminum alloys. In the current study, an uncoupled fracture criterion (Group III) is used to predict failure of magnesium alloy sheet at room temperature. A mean-field crystal plasticity model with

visco-plastic self-consistent formulation (denoted hereinafter as VPSC) is chosen to replace the phenomenological plasticity model required. [32–34]. This replacement bears the advantage of accounting for the crystallographic texture and its evolution; hence the plastic anisotropy induced by grain orientation is intrinsically included. The VPSC model is relatively efficient yet is capable of capturing various macro-mechanical features reflecting distinctive micro-mechanical mechanisms pertaining to magnesium alloys, which are not easily captured in the phenomenological plasticity models. The superior predictive capability of the VPSC formulation has been validated on various magnesium alloys [16,35–37]. Moreover, the same model has been extended for Group I criteria using the Marciniak-Kuczyński (MK) approach, which has been successfully applied for magnesium alloys as well. Hence, the mean-field VPSC model as a stand-alone numerical code is expected to provide an effective and adequate description of plastic deformation.

It should be mentioned that the self-consistent crystal plasticity model can be employed in the full field framework to provide spatially resolved stress-strain fields as shown in [38,39]. A study by Lebensohn et al. [40] is also worth noting since the VPSC formulation is extended to address the presence of void and its effects on plastic behavior of polycrystalline aggregate, which corresponds to Group II criterion. However, the full field computation per se requires intensive computational resources thus is not considered in the current study. The mentioned VPSC model extended for porous plasticity requires a separate treatment on triaxiality, and the Group II criterion is not considered in the current study.

Since the mean field VPSC model has not been utilized for Group III criteria before, its validity needs to be shown, which motivated the current study. The scope of investigation is confined to demonstration on the validity and the effectiveness of a new uncoupled fracture criterion based on a simple damage indicator. The criterion is calibrated only for uniaxial tension tests and the validity is investigated through applications for various mixed-mode deformation histories realized on the basis of the Arcan tests. Although, from the macroscopic point of view, edge failure appears in all tested cases, a detailed analyses of the local stress triaxiality is performed.

2 Material and Experiments

A commercial magnesium alloy known as E-form [41] produced by POSCO via twin roll casting was chosen for the investigation. The alloy is referred hereinafter as AZ31, which is a more common name based on its chemical composition (Mg + 3%Al + 1%Zn). The as-received sheet has a thickness of 1.2 mm and has been fully recrystallized showing an average grain size of 11 μm . The sheet exhibits a strong initial crystallographic texture, which is typically characterized by the preferential alignment of (0002) basal pole along the normal direction of the sheet. Test specimens were cut from the as-received sheet finished by electrical discharge machining. Uniaxial tension and Arcan tests were conducted in order to calibrate parameters for the failure criterion and the VPSC model; and to validate the failure criterion, respectively.

2.1 Uniaxial tension tests

Typical dog-bone tensile test specimens following the common standards (parallel length 65 mm and width 16 mm) were cut along the rolling direction (RD), diagonal direction (DD), and the transverse direction (TD), which can be also denoted by the respective angles (i.e., 0°, 45° and 90°) from the RD. For each direction, the uniaxial tension tests were repeated for five specimens. The top surface of specimen was sprayed prior to testing with black speckles on a white painted layer to acquire the evolution of displacement fields via digital image correlation (DIC) technique. The digital images were collected using a stereo camera system (Aramis by GOM) to permit the DIC analysis using the three-dimensional displacement vector field. The specimen was mounted on a universal testing machine with a loadcell capacity of 63 kN. The crosshead speed was set to 2 mm/min, which corresponds to an initial strain rate of $5 \times 10^{-4} \text{ s}^{-1}$. Load signals and the digital images were acquired with a frequency of 20 Hz.

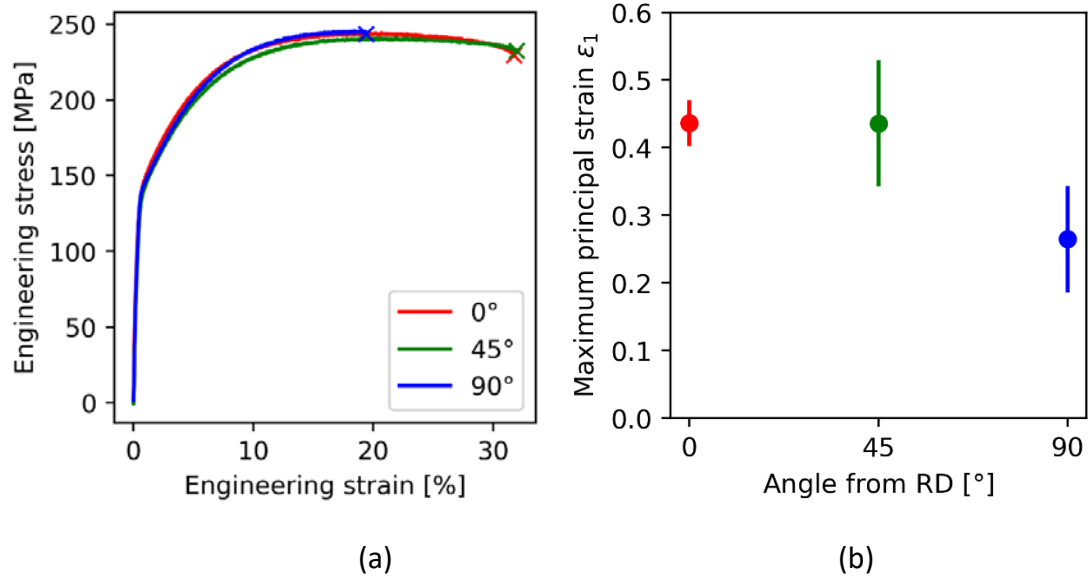


Figure 1 (a) Engineering stress-strain curves for three different sample orientations, namely, 0°, 45°, and 90° from the rolling direction, which can be also denoted as RD, DD, and TD; (b) Maximum principal strain at fracture resulting from the uniaxial tension tests along the three directions.

The engineering stress vs. engineering strain curves resulting from uniaxial tension tests are shown in Figure 1a. The reproducibility of the tests was excellent; hence in Figure 1a only one representative test result for each orientation is included. The engineering strain was measured using displacement between two separate points aligned along the loading direction. The engineering stress vs. engineering strain curves up to uniform elongation are fairly isotropic. The strain at failure, however, exhibits a directional dependence in that the failure strain along TD is significantly lower than the other two orientations. Total elongations larger than 30% were obtained along the RD and DD, while that along TD amounted to a value less than 20%. Irrespective of the tensile direction, the specimens failed after diffuse necking with separation aligned perpendicular to the tensile direction, see Figure 2. This implies that the Group I criterion (the instability criterion with the inclined localization band) is not adequate for the current magnesium alloy, since it will not represent the physical mechanisms leading to failure.

For the analyses on fracture behavior, the local strain quantities at the failure initiation point and its neighborhood are required. To that end, the facet point of pixels closest to the point of crack initiation was manually determined from the last recorded digital image prior to crack. The in-plane components of the deformation gradient were computed by the Aramis software as a user-defined field and exported as a function of time. More detailed procedure to derive other quantities (such as strain and rotation) from the deformation gradient tensor will be discussed in Section 2.3. Figure 1b shows the variation of the maximum principal strains obtained at the position of cracking (using the logarithmic strain measure) with respect to the tensile directions. Considering that a logarithmic strain is smaller than its corresponding engineering strain measure, the value of local strain shown in Figure 1b is higher than what is visible in Figure 1a. Therefore, the larger true strain implies that the fracture occurred in a localized region, which however does not form a strain-localization band (as opposed to the assumption required in Group I criterion using MK approach).

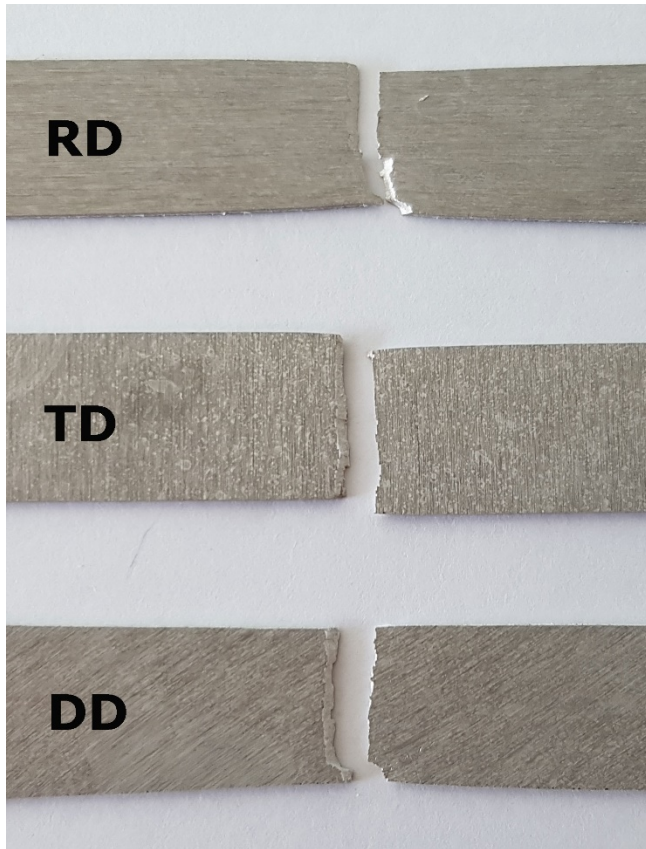


Figure 2 macroscopic view on the fracture surfaces of the tensile samples showing diffuse necking and separation perpendicular to the loading direction

2.2 Arcan tests

A modified Arcan fixture was employed to the universal testing machine to impose a mixed-mode loading. It consists of a notched sheet sample clamped in a holder, which was set to positions 0° , 15° , 30° , 45° , and 60° from the vertical axis parallel with the loading direction. The fixture as well as the test setup were described earlier in [42]. A sketch showing the fixture and the sample is reproduced in Figure 3. Two separate sets of test configurations were considered, namely RD and TD configurations. In the RD configuration, the notch of the specimen shown in Figure 3 is aligned perpendicular to the RD, and vice versa for the TD configuration. The samples were cut using electrical discharge machining (EDM), in order not to introduce local microstructural changes to the material. For each of the RD and TD configurations, a tilting of specimen with respect to the loading direction can be imposed, which is quantified by the angle θ as shown in Figure 4. The test matrix of the Arcan tests utilized for the current investigation are summarized in Table 1.

The deformation history of fractured site was obtained using the same DIC technique applied to uniaxial tension test (Section 2.1). All the samples failed by crack initiation followed by crack extension of several millimeters. Generally, the cracks initiated in the notch region at the free edge.

Table 1 Test matrix of the modified Arcan tests [42]

Tilting angle θ (see Figure 4)	0°	15°	30°	45°	60°
RD configurations	3 tests	3 tests	3 tests	3 tests	3 tests
TD configurations	3 tests	3 tests	3 tests	3 tests	3 tests

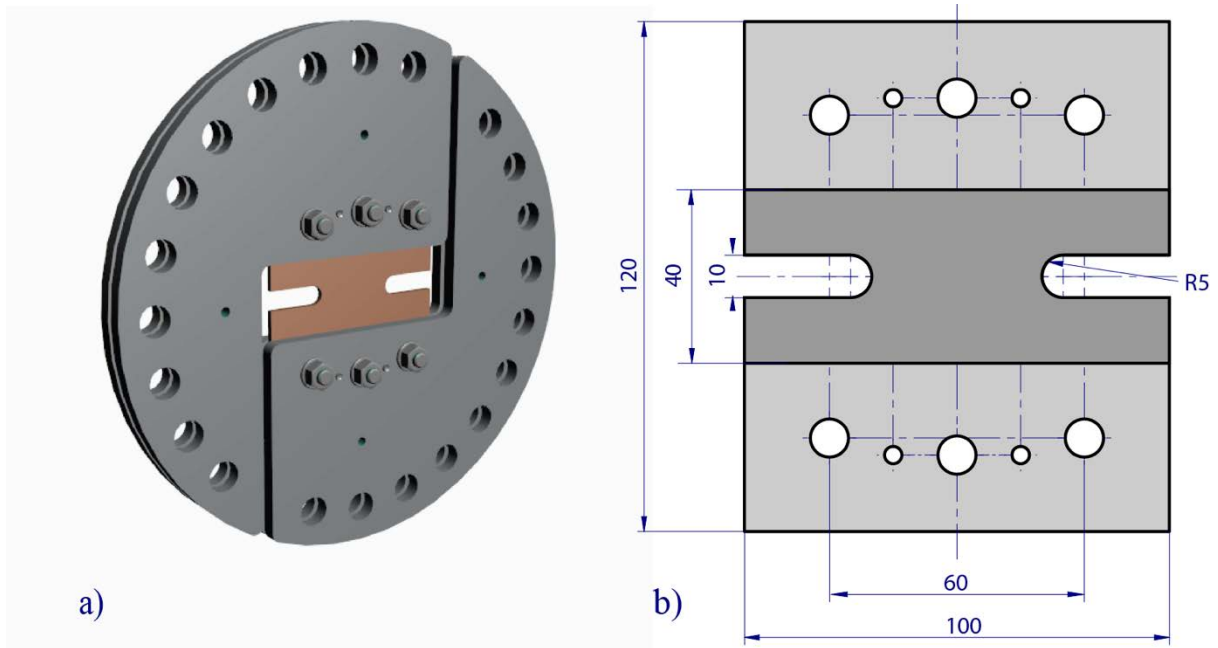


Figure 3 Fixture with mounted sheet sample in the 0° - configuration (a), and specimen dimension in millimeters (b)

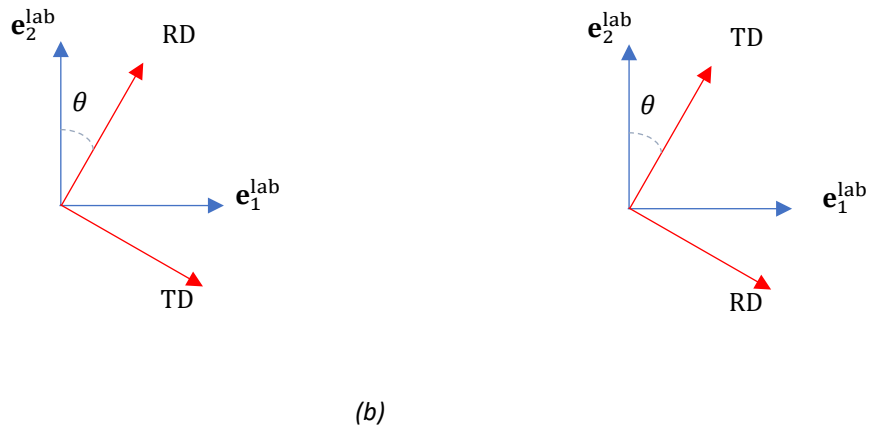
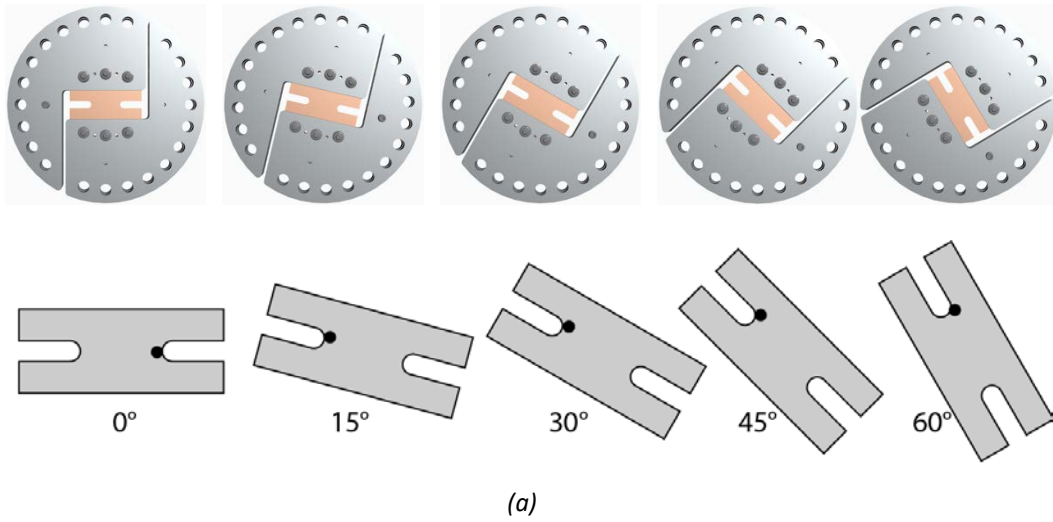


Figure 4 (a) Arcan tests conducted with six configurations for each RD/TD alignment along loading direction (i.e., e_2^{lab}); (b) Misalignment between the laboratory axes (e_1^{lab} , e_2^{lab}) and material axes (RD, TD) is permitted by a tilting angle θ : the tilting angle defined for RD and TD configurations is shown on left and right, respectively.

2.3 DIC to obtain deformation states

During the experimental tests presented in Sections 2.1 and 2.2, digital images were taken in-situ and were saved together with the load signal on a hard disk with 2 Hz via a ring buffer. This technique allows recording the digital images with an acquisition frequency of 20 Hz towards the onset of material failure. As mentioned earlier in Section 2.1, the site of fracture is assumed to be a spatial point that is manually determined and is as close as possible to the crack initiation site. The displacement field around the fracture site, from which the deformation gradient tensor (i.e., the derivative of displacement with respect to the spatial coordinate) was estimated, was analyzed by the DIC software. The multiplicative decomposition is applied to the deformation gradient tensor pertaining to the site of fracture in order to obtain the strain and the rotation tensors. In both mechanical tests presented in Sections 2.1 and 2.2, the two in-plane axes of laboratory coordinates (denoted by $\mathbf{e}_1^{\text{lab}}$ and $\mathbf{e}_2^{\text{lab}}$ shown in Figure 4b) are used as the reference frame, while the axis 3 ($\mathbf{e}_3^{\text{lab}}$) aligns with the thickness of the sheet.

F_{11}, F_{12}, F_{21} and F_{22} components of the deformation gradient tensor \mathbf{F} at the initiation site can be obtained from the above analysis. However, the other components associated with the thickness direction (namely $F_{13}, F_{23}, F_{31}, F_{32}$ and F_{33}) cannot be experimentally determined from the current DIC technique. To that end, the assumption of incompressibility was applied while discarding the thickness related shear components. The determinant of the matrix form of \mathbf{F} is related to the volume change such that:

$$\frac{dv}{dV} = \det(\mathbf{F}) \quad \text{Eq. 1}$$

where dv and dV are the volume elements before and after the incremental deformation. According to the incompressibility condition (i.e., $dv = dV$), the determinant $\det(\mathbf{F})$ equals to 1. In addition, discarding the thickness shears, i.e., $F_{13} = F_{31} = F_{23} = F_{32} = 0$, the Eq. 1 becomes:

$$\det(\mathbf{F}) = 1 = F_{11}F_{22}F_{33} - F_{12}F_{21}F_{33} = F_{33}(F_{11}F_{22} - F_{12}F_{21}). \quad \text{Eq. 2}$$

As a result, $F_{33} = 1/(F_{11}F_{22} - F_{12}F_{21})$.

It should be noted that the resulting deformation gradient tensor in an incremental form may contain a significant amount of noise. To reduce the experimental noise, Savitzky-Golay filter [43] as implemented in SciPy package [44] was applied to the deformation gradient. A

series of discrete F_{ij} values obtained from a batch of sequential images is fitted to a polynomial function with respect to time steps. Apparently, the degree of smoothing is affected by 1) the number of sequential images in a batch (i.e., the binning size); and 2) the order of polynomial used. The smoothed \mathbf{F} tensor signal provides the boundary condition loaded in the VPSC calculation (Section 3.1). As a result, the stress response from VPSC calculation is affected by the degree of smoothing pertaining to the Savitzky-Golay filtering. Therefore, an appropriate binning size should be carefully determined: batches with a smaller number of images led to a noisy stress response whereas batches with too many images would lead to overfitting. Based on a parametric study presented in the Appendix, an appropriate binning size and the polynomial order were determined. In the following, the smoothed deformation gradient tensor is used, unless otherwise noted.

The smoothed deformation gradient is multiplicatively decomposed to stretch \mathbf{U} and rotation \mathbf{R} tensors such that:

$$\mathbf{F} = \mathbf{U} \cdot \mathbf{R} . \quad \text{Eq. 3}$$

The engineering strain tensor ϵ is obtained as:

$$\epsilon_{ij} = U_{ij} - \delta_{ij} , \quad \text{Eq. 4}$$

where δ_{ij} is the Kronecker delta. The logarithmic strain tensor ϵ is obtained as below:

$$\epsilon_{ij} = \delta_{ij} \ln(1 + \epsilon_{ij}) + (1 - \delta_{ij})\epsilon_{ij}.$$

The rate of rotation $\dot{\mathbf{R}}$ is estimated by

$$\dot{R}_{ij}^{(n+1)} = \frac{R_{ij}^{(n+1)} - R_{ij}^{(n)}}{t^{(n+1)} - t^{(n)}} , \quad \text{Eq. 5}$$

in which the superscripts $(n + 1)$ and (n) denote the time steps corresponding to the moments of image acquisition. The same was applied to obtain the logarithmic strain rate $\dot{\epsilon}$.

3 Modelling

3.1 Visco-plastic self-consistent crystal plasticity model

While through the DIC measurements the strain states on the sample surface are determined, the stress states remain unknown so far. To fill this gap, the mean-field VPSC model was chosen as the constitutive model in this study. In this section, only a brief description on the VPSC model is given. Readers are directed to [45] for more details on the VPSC crystal plasticity model.

According to the VPSC formalism, each individual grain is treated as an inclusion embedded in an effective homogeneous medium [46] and follows the visco-plastic constitutive law as below:

$$\dot{\varepsilon}_{ij}^{vp} = \dot{\gamma}_0 \sum_s \mathbb{m}_{ij}^s \left(\frac{\mathbb{m}_{kl}^s \sigma_{kl}}{\tau_0^s} \right)^n \quad \text{Eq. 6}$$

where \mathbb{m}^s , $\dot{\gamma}^s$, τ_0^s and $\dot{\gamma}_0$ are the Schmid tensor, the shear rates, the critical resolved shear stress, and the normalizing factor, respectively; The symbols $\dot{\varepsilon}^{vp}$ and σ denote the visco-plastic strain rate and stress tensors pertaining to an individual grain. The Schmid tensor \mathbb{m}^s is defined by the slip (or twin) plane normal \mathbf{n} and direction \mathbf{b} such that: $\mathbb{m}_{ij}^s = \frac{1}{2} (n_i^s b_j^s + n_j^s b_i^s)$. The superscript 's' appended to \mathbb{m} , \mathbf{n} , \mathbf{b} and τ_0 is to denote that the associated term pertains to individual slip system. The strain hardening behavior is described by permitting the evolution of the critical resolved shear stress through:

$$\tau_0^s = \tau_0 + (\tau_1 + \theta_1 \Gamma) \left(1 - \exp \left(-\Gamma \left| \frac{\theta_0}{\tau_1} \right| \right) \right), \quad \text{Eq. 7}$$

where τ_0 , τ_1 , θ_0 , and θ_1 are the hardening parameters, and $\Gamma = \sum_s \Delta \gamma^s$ is the accumulated shear strain in the grain [47]. The equivalent inclusion method [46,48] for visco-plastic inclusion embedded in visco-plastic matrix [45,49] leads to the macroscopic visco-plastic constitutive description:

$$\bar{\varepsilon}_{ij}^{vp} = \bar{\mathbb{M}}_{ijkl}^{vp} \bar{\sigma}'_{kl} + \bar{\varepsilon}_{ij}^{0,vp}, \quad \text{Eq. 8}$$

where $\bar{\sigma}'$ and $\bar{\varepsilon}^{vp}$ are the overall (macroscopic) deviatoric stress and strain tensors, respectively; and $\bar{\mathbb{M}}^{vp}$ and $\bar{\varepsilon}^{0,vp}$ are the macroscopic visco-plastic compliance and back-extrapolated term, respectively.

It should be mentioned that the macroscopic properties, $\bar{\mathbb{M}}^{vp}$ and $\bar{\varepsilon}^{0,vp}$, are functions of micromechanical properties including the Voce hardening parameters in Eq. 7, the

crystallographic texture, crystal structure and slip systems. The macroscopic properties are priori unknowns and are iteratively determined for a given state. As crystallographic texture evolves, these quantities are updated so that the evolution of anisotropy induced by slip and twinning activity is realistically captured. Note that in the current investigation the loading conditions for VPSC simulation are fully described by strain rate and spin rate tensors, namely, $\dot{\boldsymbol{\varepsilon}}$ and $\dot{\boldsymbol{R}}$ obtained from DIC data – see Section 2.3. The overall deviatoric strain tensor is fully described as below:

$$\bar{\boldsymbol{\varepsilon}}_{ij}^{vp} = \begin{bmatrix} \dot{\varepsilon}_{11}^{(DIC)} & \dot{\varepsilon}_{12}^{(DIC)} & 0 \\ \dot{\varepsilon}_{12}^{(DIC)} & \dot{\varepsilon}_{22}^{(DIC)} & 0 \\ 0 & 0 & -\dot{\varepsilon}_{11}^{(DIC)} - \dot{\varepsilon}_{22}^{(DIC)} \end{bmatrix} \quad \text{Eq. 9}$$

where the components with the superscript (DIC) are experimental data obtained via the method present in Section 2.3. Since the boundary condition is fully described in terms of strain rate, all components of deviatoric stress tensor $\bar{\boldsymbol{\sigma}}'$ result from model-calculation. Consequently, the resultant stress response may contain non-zero lateral components even when the DIC strain rate of uniaxial loading is used in Eq. 9 unless the predictive accuracy of the VPSC model is flawless.

3.2 Linear transformation of strain

The anisotropy of fracture strain evident in Figure 1b is described on the basis of a linear transformation of the strain referred in the orthotropic material axes. The strain components referred in the material axes are linearly transformed, similar to the way that the transformed stress tensor is used in the anisotropic yield functions [50,51]. To account for the loading history, an incremental form is used. In the most general way, such an idea can be formulated to

$$\tilde{\boldsymbol{\varepsilon}}_{ij} = \mathbb{L}_{ijkl} \dot{\boldsymbol{\varepsilon}}_{kl} \cdot \quad \text{Eq. 10}$$

A similar approach was reported in [14,27,30,31], where the equivalent plastic strain quantity for the phenomenological plasticity model was obtained from the transformed strain rate $\tilde{\boldsymbol{\varepsilon}}$. Care should be taken as the material may undergo a significant amount of spin so that the material rotates away from the initial orientation. In that case, the spin tensor $\dot{\boldsymbol{R}}$ resulting from the polar decomposition of deformation gradient tensor should be properly

accounted for in order to ensure that the strain rate components $\dot{\epsilon}_{ij}$ are consistently referred in the orthotropic material axes.

Considering that only $\dot{\epsilon}_{11}$, $\dot{\epsilon}_{22}$, and $\dot{\epsilon}_{12}$ components are significant in the current experimental set-up, the following matrix form of Eq. 10 is assumed sufficient:

$$\begin{bmatrix} \tilde{\epsilon}_{11} \\ \tilde{\epsilon}_{22} \\ \tilde{\epsilon}_{12} \end{bmatrix} = \begin{bmatrix} \mathbb{L}_{11} & 0 & 0 \\ 0 & \mathbb{L}_{22} & 0 \\ 0 & 0 & \mathbb{L}_{66} \end{bmatrix} \begin{bmatrix} \dot{\epsilon}_{11} \\ \dot{\epsilon}_{22} \\ \dot{\epsilon}_{12} \end{bmatrix}. \quad \text{Eq. 11}$$

The strain rate $\tilde{\epsilon}$ is regarded as a deviatoric quantity so that $\tilde{\epsilon}_{33} = -(\tilde{\epsilon}_{11} + \tilde{\epsilon}_{22})$. The three principal components, namely, $\tilde{\epsilon}_I$, $\tilde{\epsilon}_{II}$ and $\tilde{\epsilon}_{III}$, are used to define a damage indicator D^ϵ such that

$$D^\epsilon = \int H(\tilde{\epsilon}_I) \tilde{\epsilon}_I + H(\tilde{\epsilon}_{II}) \tilde{\epsilon}_{II} + H(\tilde{\epsilon}_{III}) \tilde{\epsilon}_{III} dt, \quad \text{Eq. 12}$$

where H denotes the Heaviside function. The time integration should be numerically performed due to the discrete nature of the data obtained from DIC measurements such that

$$D^\epsilon = \sum_i^n \left[H(\tilde{\epsilon}_I^i) \tilde{\epsilon}_I^i + H(\tilde{\epsilon}_{II}^i) \tilde{\epsilon}_{II}^i + H(\tilde{\epsilon}_{III}^i) \tilde{\epsilon}_{III}^i \right] (t^i - t^{i-1}) \quad \text{Eq. 13}$$

in which the superscript i denotes the time step.

The transformation matrix \mathbb{L} can be calibrated by minimizing the objective function defined as:

$$f(\mathbb{L}) = D^\epsilon(\mathbb{L}) - 1. \quad \text{Eq. 14}$$

In an ideal case, the damage indicator D^ϵ reaches 1 at fracture. One can extend the above for a set of multiple experimental data, for which the following objective function can be used:

$$F(\mathbb{L}) = \left\{ \sum_i (D_i^\epsilon(\mathbb{L}) - 1)^2 \right\}^{0.5} \quad \text{Eq. 15}$$

where the index i for summation denotes the individual experimental data set; 15 uniaxial tension data sets (3 directions \times 5 repeated tests for each direction) were used to calibrate the matrix \mathbb{L} using Simplex method [52]. The respective components of the transformation matrix are listed in Table 3. According to Figure 5, the damage indicator D^ϵ reaches the value of 1 regardless of uniaxial tension direction. This implies that the failure model is able

to describe the anisotropy in fracture strain of the tensile tests along RD, TD and DD, since $D^\varepsilon = 1$ refers to the status “broken”.

Table 2 Voce hardening parameters (Eq. 7) calibrated for the magnesium alloy

	τ_0 [MPa]	τ_1 [MPa]	θ_0 [MPa]	θ_1 [MPa]
Basal	41.1	50.6	276	4.41
Prismatic <a>	109	70.1	211	1.05
Pyramidal <c+a>	138	75.0	663	13.9
Tensile Twinning	30.4	0	0	0

Table 3 Linear transformation calibrated by uniaxial tension experiments.

\mathbb{L}_{11}	\mathbb{L}_{22}	\mathbb{L}_{66}
1.921	3.652	1.866

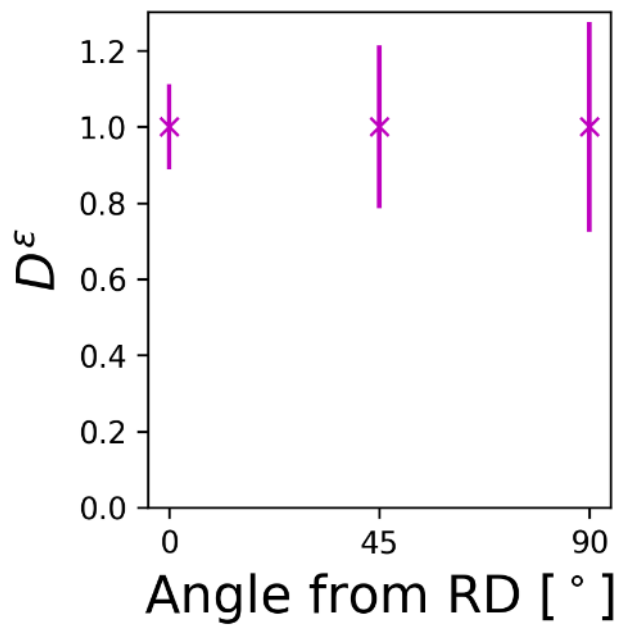


Figure 5 Damage indicators after calibration using uniaxial tension tests including the respective scatter

3.3 Stress triaxiality from VPSC

The stress triaxiality is calculated from the stress states resulting from VPSC simulations. The resulting stress tensors from VPSC are 5 dimensional deviatoric – see Eq. 8. The material response taken from the speckle pattern on the surface of the specimen fulfills the plane-stress condition ($\bar{\sigma}_{33} = 0$), from which the hydrostatic pressure p can be estimated: $p = -\frac{1}{3}(\bar{\sigma}_{11} + \bar{\sigma}_{22})$. Consequently, the Cauchy stress can be obtained using the hydrostatic pressure together with the deviatoric stress tensor resulting from VPSC. The stress state of individual grain affected by this treatment is negligible, which was verified by comparison with an elasto-visco-plastic model [53]. Therefore, the full 6 dimensional Cauchy stress obtained from VPSC using the plane-stress state is reasonable. Once the full Cauchy stress state is obtained by $\bar{\sigma}_{ij} = \bar{\sigma}'_{ij} + p\delta_{ij}$, the triaxiality η results from:

$$\eta = p/\bar{\sigma}^{eq} \quad \text{Eq. 16}$$

The equivalent stress $\bar{\sigma}^{eq}$ is assumed to be that of von Mises, which can be estimated by $\bar{\sigma}^{eq} = \sqrt{3J_2}$. The symbol J_2 denotes the second invariant of deviatoric stress tensor so that $J_2 = \frac{1}{2}\bar{\sigma}'_{ij}\bar{\sigma}'_{ij}$.

The loading history pertaining to the fracture site gives the full deformation gradient history with the help of incompressibility condition in Eq. 1. The strain rate $\bar{\dot{\epsilon}}$ and rotation rate $\dot{\mathbf{R}}$ are imposed to the visco-plastic polycrystalline aggregate, from which the evolution of the stress triaxiality η is obtained. Since the stress states investigated in the current study do not significantly change over the loading history, an averaged triaxiality should be sufficiently representative, estimated as follows:

$$\bar{\eta} = \frac{1}{T} \int_0^T \eta(t) dt \approx \frac{1}{T} \sum_i^n \frac{(\eta^i + \eta^{i-1})(t^i - t^{i-1})}{2} \quad \text{Eq. 17}$$

where T is the time when the fracture occurs and the superscripts i and n denote the discrete time steps and the final time step at the fracture, respectively.

3.4 VPSC model calibration

The initial crystallographic texture of as-received sample was obtained by electron backscattering diffraction (EBSD). A population of 1904 discrete orientations was extracted from orientation distribution considering complete grains only and omitting edge grains cut by the boundaries of the scanned field. Figure 6 shows the basal and prismatic pole figures on the basis of the selected orientations. Voce hardening parameters τ_0 , τ_1 , θ_0 and θ_1 for slip and twin systems were calibrated by fitting the uniaxial flow stress-strain curves and the R-value evolutions using a Levenberg-Marquardt optimization scheme. During parameter calibration and subsequent VPSC simulations, the rate sensitivity exponent is set to 20 for all slip and twinning systems. The result of the fit is shown in Figure 7 and the identified parameters are summarized in Table 2. Since the tensile twinning is not expected to be active by the loading conditions explored in the current study (Section 2.1 and 2.2), the critical resolved shear stress τ_0 was roughly estimated as three quarters of that for basal slip. This turned out to be necessary, as the flow stress resulting from an in-plane compression should render a lower yield stress compared to that from a tensile condition. The simulated compressive stress-strain curve included in Figure 7 hence exhibits the typical sigmoidal flow curve with a low initial yield stress (SD effect) observed for similarly textured magnesium alloys – see, e.g., [37,54].

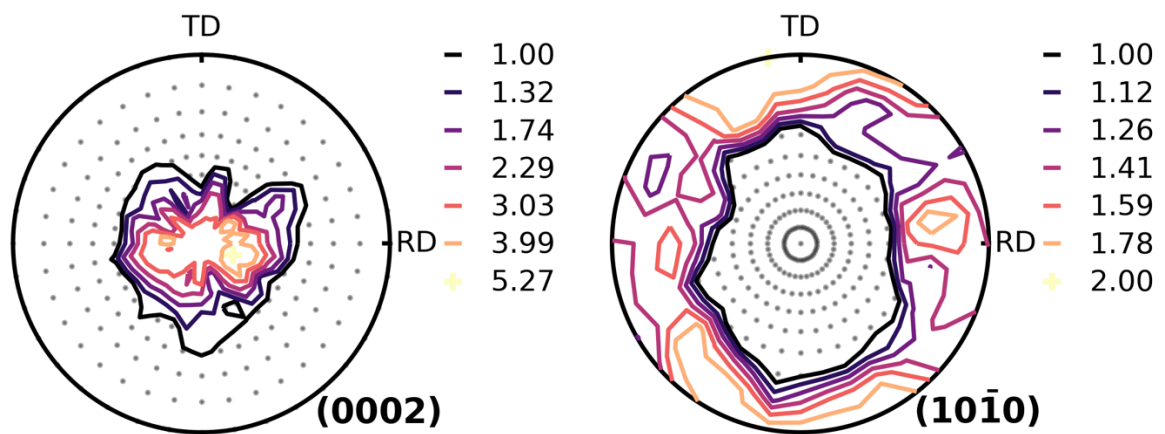


Figure 6 (0002) and (10 $\bar{1}$ 0) pole figures from the population of discrete orientations used in the VPSC model.

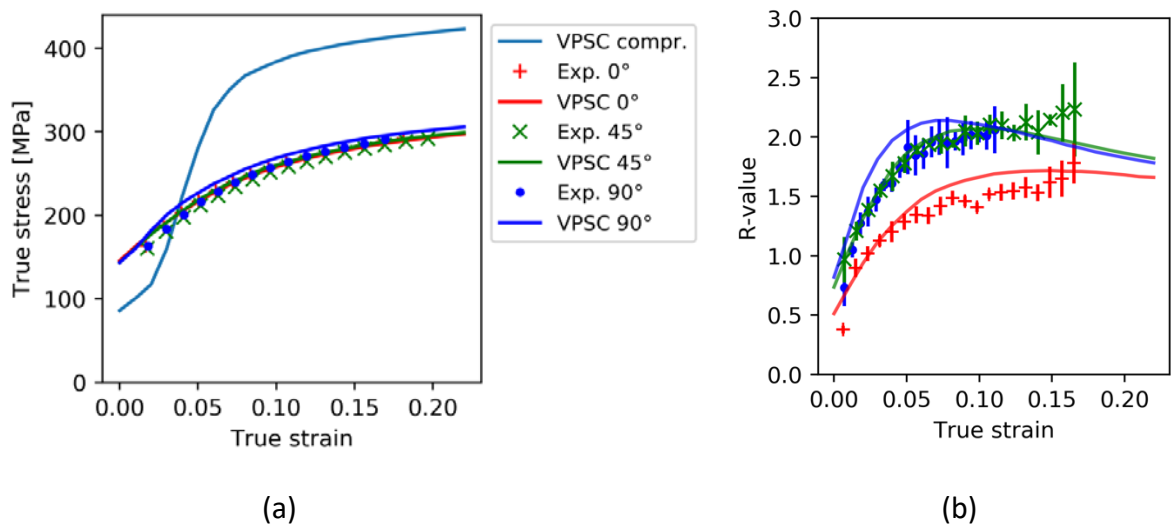


Figure 7 Experimental and VPSC-calculated (a) stress strain curves; and (b) instantaneous R-value evolution with respect to axial strain.

4 Results

4.1 Stress responses

The VPSC model calibrated in Section 3.4 is fed with the loading conditions characterized by the deformation gradient pertaining to the failure points. Figure 8 gives the VPSC-calculated stress evolutions with respect to time for each Arcan test tabulated in Table 1. In it, the stress tensor components are referred in the laboratory axes as described earlier in Figure 4. Each test result within individual subplot in Figure 8 is distinguished by a symbol (squares, circles and crosses) attached to the end of curve (i.e., the fracture point). Overall, the calculated stress responses for the three repeated loading histories led to consistent results. In certain stress evolution curves, e.g., the TD 0° case with square, the level of stress oscillation seems exceedingly large. The large oscillation attributes to the presence of noise still remaining in the smoothed deformation gradient using the Savitzky-Golay filter. Nevertheless, later it is shown that this level of noise has only a marginal effect on the results of the current investigation.

By increasing the θ angle of Arcan specimen defined in Figure 4, the orthotropic material axes tilt away from the laboratory axes so that a mixed-mode loading can be induced. Tilting of material axes by the angle θ together with the material rotation described by the tensor \mathbf{R} may lead to a significant amount of shear and lateral stress components ($\bar{\sigma}_{12}$ and $\bar{\sigma}_{11}$), see Figure 8.

Figure 9 shows the evolution of the stress triaxiality η determined by Eq. 16 for each repeated test together with the averaged triaxiality $\bar{\eta}$ (Eq. 17) denoted by a horizontal red line. The noise in η evolution seems significant, which apparently inherits from the oscillation in stress responses shown in Figure 8. The averaged triaxiality renders a single value for each test since it results from a time integration. In all Arcan tests, its value is above the theoretical value of 1/3 expected at the edge. As evidenced in Figure 9, the respective values lie between 0.37 and 0.41, with the tendency of higher average triaxialities in case of RD samples than in case of TD counterparts.

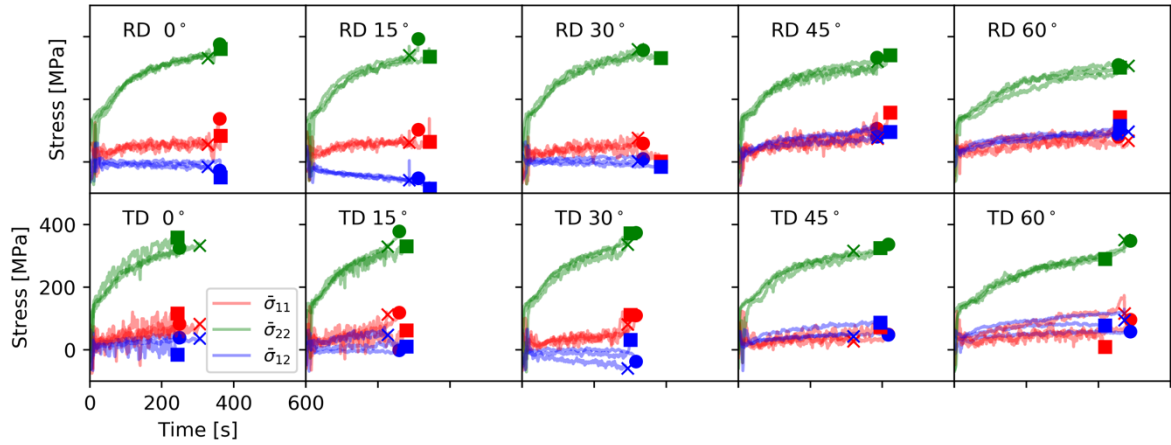


Figure 8 Stress evolution resulting from VPSC simulations for the Arcan tests. The stress components are referred to the laboratory axes defined in Figure 4.

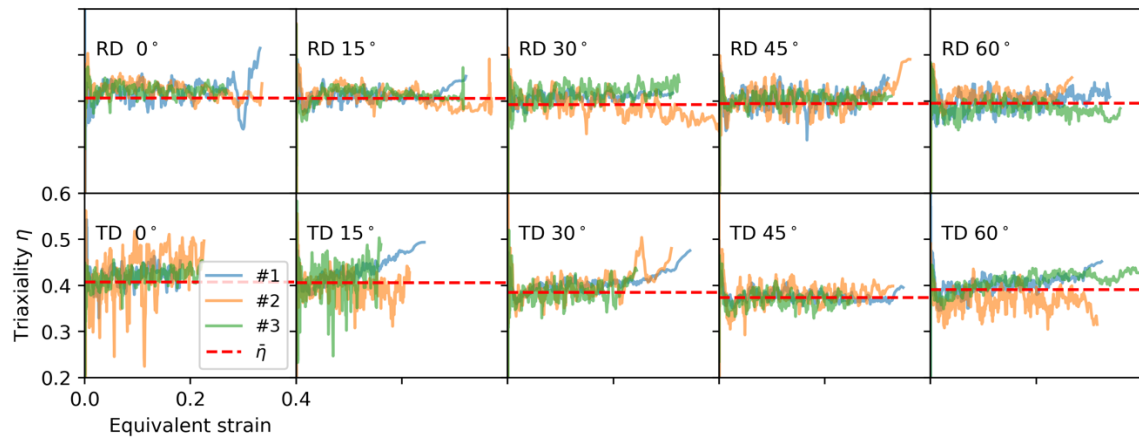


Figure 9 Evolution of triaxiality η calculated by VPSC stress calculation; The broken red line gives the average of $\bar{\eta}$ (Eq. 17) for each Arcan configuration tabulated in Table 1.

4.2 Failure strains and damage indicator

Figure 10 shows that the maximum principal strains at failure resulting from the Arcan tests. For RD configurations it amounts to around 0.32 regardless of the tilting angle θ . In the case of TD configurations, however, the strain at failure rises with an increase in θ . Overall, the TD samples fail at a lower strain compared to the RD samples, except at $\theta = 60^\circ$. The anisotropy in failure behavior evident in Figure 10 is in line with the observations on tensile tests (Figure 1b), where the TD samples show a significantly lower maximum principal strain than the other two loading directions.

The transformation matrix with three non-zero components (\mathbb{L}_{11} , \mathbb{L}_{22} , and \mathbb{L}_{66}) suffices to capture the anisotropic fracture of the tensile samples by using the damage indicator D^ε as shown in Figure 5. Using the same matrix, the evolution of damage indicator D^ε was evaluated for each of the Arcan loading histories, and the results are shown in Figure 11. The average D^ε values at fracture are summarized in Figure 12 with uncertainty bars corresponding to the standard deviations pertaining to the three repeated tests. In general, the evolution of D^ε is progressive, with an accelerated increase of damage indicator prior to failure of the respective sample. Figure 12 shows that the averaged value of D^ε at fracture of the Arcan samples is less than the value of 1 regardless of the test configuration. This indicates that the model renders the samples as being not fractured, which is an obvious contradiction to what the tests retrieved.

In order to better understand this contradiction, the average D^ε values at fracture are plotted as a function of the averaged stress triaxiality $\bar{\eta}$ in Figure 13 for both tensile and Arcan tests. The results in Figure 13 can be summarized to the following distinctive features:

- i. The triaxiality of uniaxial tension in the case of the tensile samples is larger than $1/3$; the $\bar{\eta} = 1/3$ is indicated by the gray vertical line.
- ii. There is a correlation between the triaxiality and D^ε at fracture for the entire data: increase in the triaxiality leads to the decrease in D^ε value at the fracture.

Regarding the 1st feature, it should be mentioned that non-zero lateral stress components could result from the VPSC simulation on uniaxial tension since the velocity gradient tensor was fully imposed as boundary condition as discussed earlier in Section 3.1. Moreover, the material may exhibit inhomogeneous stress response even inside the gauge area as demonstrated in [55], so that the stress state at the fracture site might be significantly deviated from the global uniaxial stress state. Furthermore, the point at which the

deformation gradient was calculated lies a few microns away from the edge, since the respective facet used to calculate the displacement gradient cannot be located exactly at the edge. Diffuse necking hence leads to a small increase of triaxiality.

The 2nd feature on the presence of a correlation between D^ε and $\bar{\eta}$ is further investigated in Figure 14a, where the D^ε vs. $\bar{\eta}$ coordinates are fitted to a linear function $D^*(\bar{\eta})$ denoted as the straight line. Correspondingly, a correction to mitigate the dependency of the damage indicator on triaxiality is attempted as following:

$$D^{\varepsilon*} = D^\varepsilon - (D^*(\bar{\eta}) - 1) \quad \text{Eq. 18}$$

where $D^{\varepsilon*}$ is the ‘corrected’ damage indicator based on the linear fit $D^*(\bar{\eta})$. The corrected damage indicator D^* shown in Figure 14b then gives values fairly close to unity for all the experimental data. Interestingly, this applies to all tests considered. Since the Arcan tests along RD and TD show slightly different values of stress triaxiality, the “correction” simply based on $\bar{\eta}$ is successful considering the experimental uncertainties denoted by the error bars.

In fact, there are two main contributions to the uncertainty:

- i. The standard deviation among experimental data obtained from the repeated tests
- ii. The residual noise that cannot be completely removed from the Savitzky-Golay filter as evident in the noisy triaxiality shown in Figure 9.

While the former is regarded intrinsic to the nature of problem which might also have been originated from material inhomogeneity, the latter can be regarded as an artefact and is an unwanted contribution. Therefore, care should be taken by checking if the condition of the smoothing performed on the deformation gradient has an influence on the linear relationship between the damage indicator and the triaxiality. Despite of the evidence that the smoothing did not affect the triaxiality as shown in Appendix, we repeated the entire DIC analyses and subsequent VPSC simulations based on nearly an *overfitting* condition. The data in Figure 15 shows that the binning size of 10% to the total number of digital images, which is twice larger than the one assumed in Figure 14. Nevertheless, the result in Figure 15 is nearly equivalent with Figure 14. Only a marginal tolerance that is smaller than the persistent error bar is shown, which implies that the smoothing of DIC data does not significantly affect the main results.

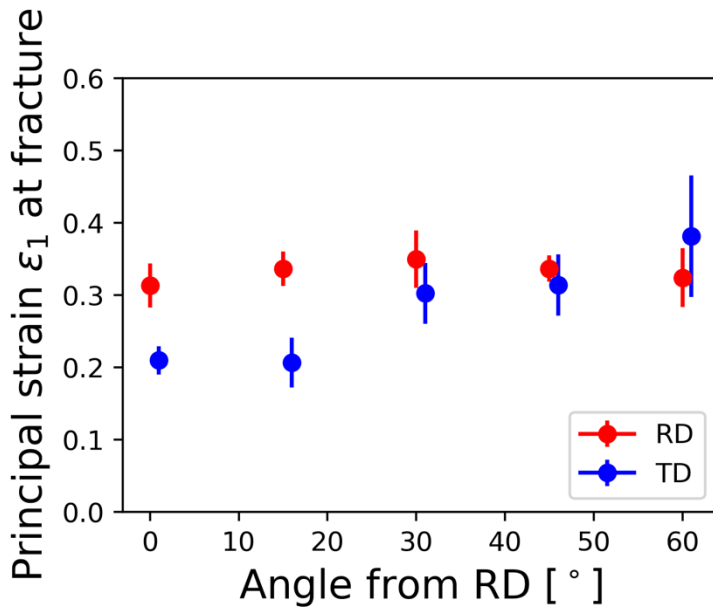


Figure 10 Principal strain at fracture from Arcan tests; TD experimental values were intentionally shifted rightward inasmuch as 1° for better visualization.

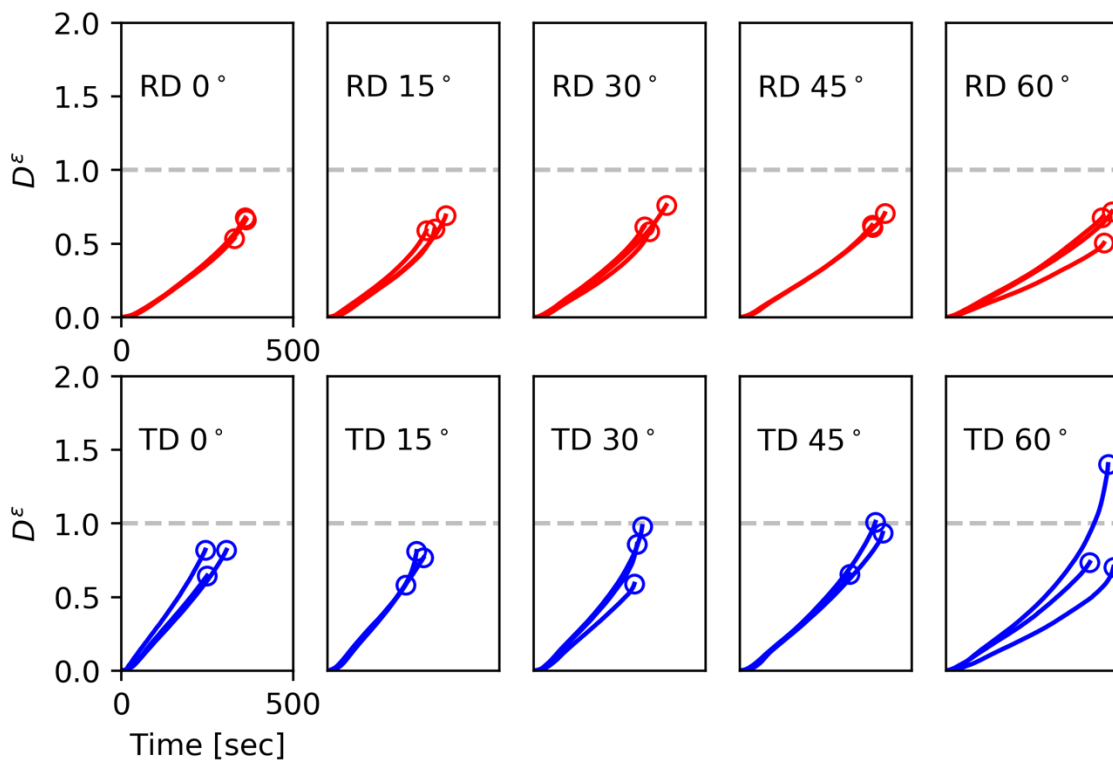


Figure 11 Evolution of D^ϵ calculated for Arcan tests until fracture.

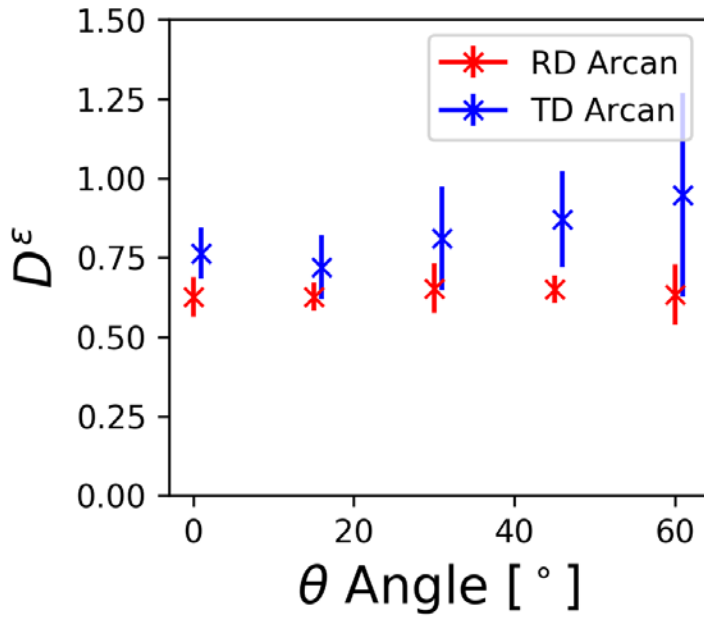


Figure 12 Damage indicators at fracture calculated for Arcan tests; TD experimental values were intentionally shifted rightward inasmuch as 1° for better visualization.

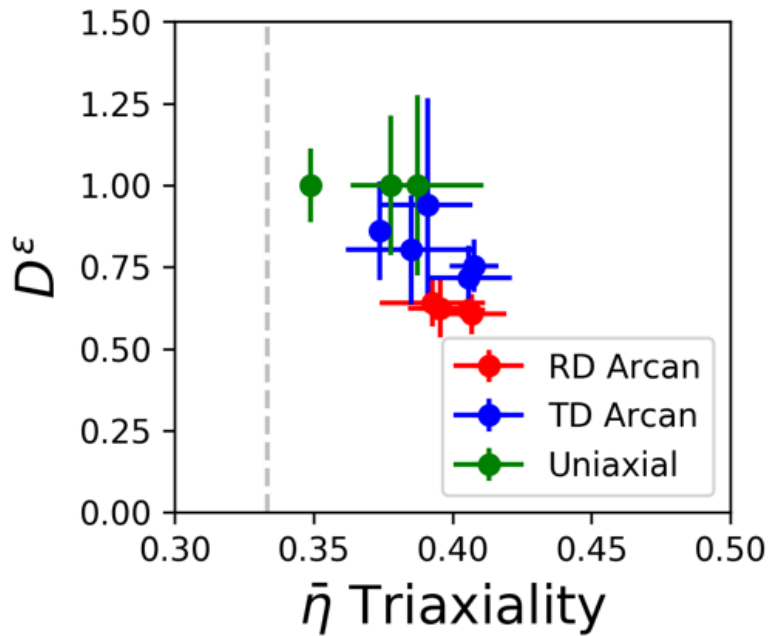


Figure 13 Damage indicators at fracture with respect to the average triaxiality $\bar{\eta}$.

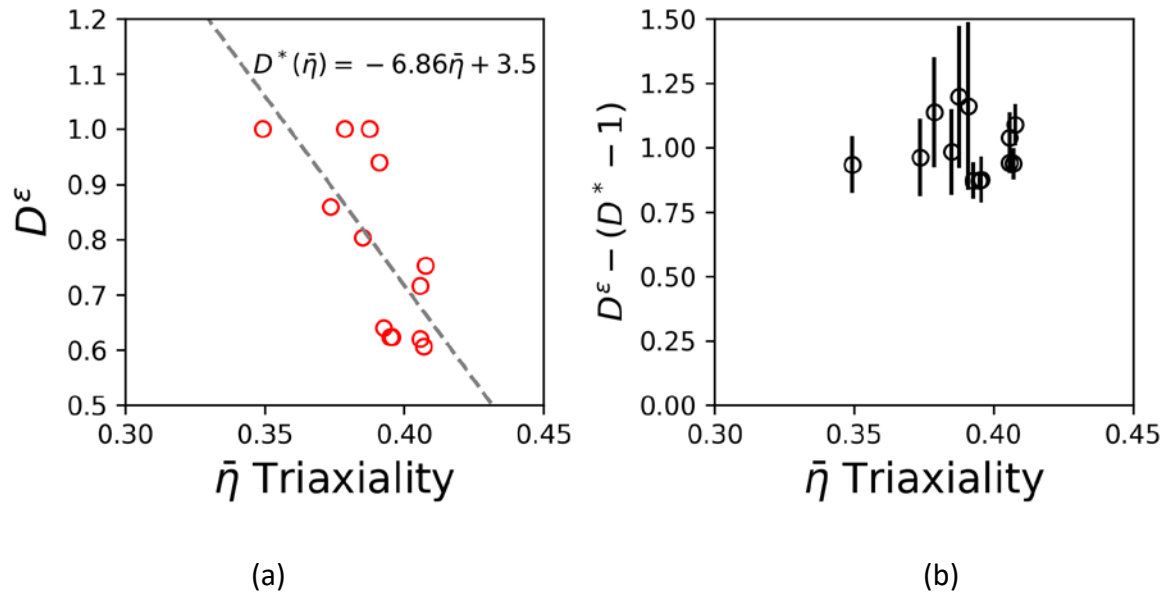


Figure 14 (a) Least square fit of D^ϵ ; and (b) corrected damage indicators using the binning size corresponding to 5% of the total number of digital images up to fracture as suggested in Appendix.

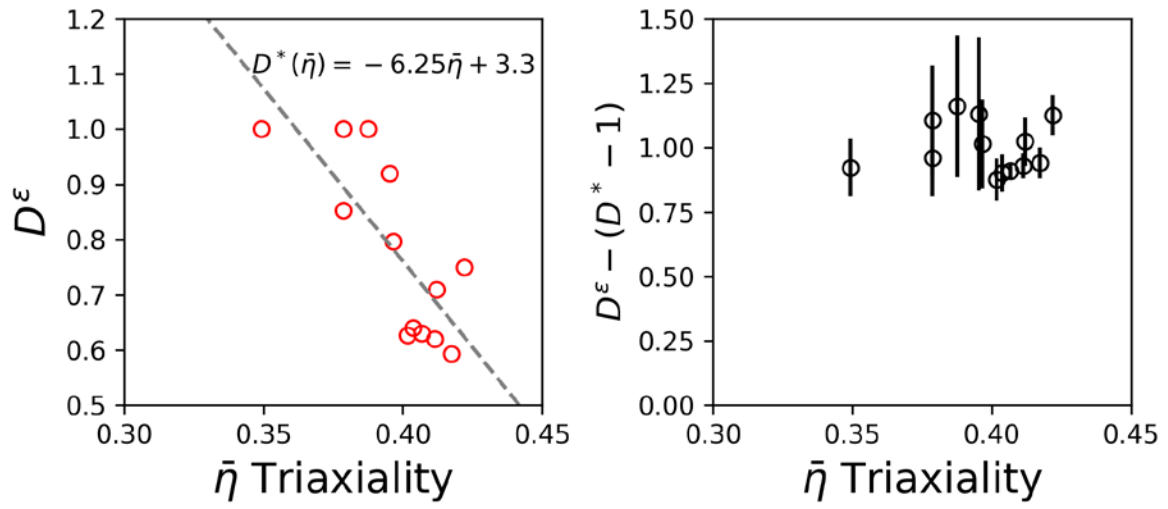


Figure 15 The results presented Figure 14 were repeated with the binning size corresponding to 10% of the total number of digital images up to fracture.

5 Discussion

5.1 General comments on linear transformation based damage indicator

The idea of using the linearly transformed strain to reflect the failure anisotropy originates from anisotropic yield functions – see for example [50,51]. The linear transformation of strain has been adapted by other studies focusing on decoupled failure criteria. For example, Luo et al.[30] and Lou and Yoon [31] used the linearly transformed strain for aluminum alloys, which has been also applied to magnesium alloys by Jia and Bai [14,27]. In the mentioned studies, the transformed strain was used to obtain the equivalent plastic strain that is employed to phenomenological plasticity models.

In the current approach, the transformed strain is directly used to quantify the damage accumulated by plastic activities through Eq. 12. Only three components of \mathbb{L} matrix were required for calibration by fitting with the three uniaxial tension tests. The damage indicator D^ε characterized by the three strain components was used to reproduce the anisotropic fracture behavior of uniaxial data as shown in Figure 5. When applied to the strain histories of Arcan samples, however, the prediction of D^ε indicator in the current form was poor – D^ε values at fracture amounted to a value noticeably less than unity (meaning no failure). This implies that the damage criterion characterized only by strain information cannot predict fracture in more general mixed mode conditions. This is somehow unexpected since failure initiates at the free edge in case of tensile and Arcan tests, where the stress state is uniaxial due to the equilibrium condition. With the common concept of triaxiality-dependent (ductile) failure caused by void growth [56–58] in mind, the detailed analysis of stress triaxiality in the current tests appears to be necessary.

In fact, the D^ε value less than unity, for the case of Arcan tests, indicates that the damage has not been sufficiently accumulated in the material. This may be attributed to the fact that the damage indicator as in the current form does not account for triaxiality of the material. It is quite well known that the increase in triaxiality promotes the void growth thus leading to an early failure, which is not accounted for the simple damage indicator assumed in the current study due to the lack of any stress measure. The presence of linear correlation between the D^ε values at fracture and the average triaxiality shown in Figure 14 therefore supports this idea. More specifically, by explicitly accounting for the influence of triaxiality via correcting the damage indicator as in Eq. 18, the damage value at fracture amounts to

unity regardless of Arcan configuration within the tolerance resulting from the repeated tests.

5.2 Validation on linear transformation method

Although the linear transformation on fracture strain has been used by others, not much detailed discussion has been given to its validity. It appears important to assess the physical interpretation of the linear transformation matrix as it bears the key function in accounting for failure anisotropy. The $\bar{\mathbb{L}}_{22}$ component has the highest value, see Table 3, which indicates that normal strain along TD ($\bar{\varepsilon}_{22}$) has the most pronounced contribution to the damage accumulation in comparison with the other strain components, namely $\bar{\varepsilon}_{11}$ (RD strain) and the shear $\bar{\varepsilon}_{12}$. The contribution of strain along different directions may be related to the crystallographic texture. In fact, the (0002) basal pole figure in Figure 6 shows that the regions of maximum intensity align with the equator, which indicates the presence of an orthotropic symmetry thus leading to dissimilar contributions: material is more ductile along RD than TD. A similar observation is reported in the literature. According to the analysis reported by Somekawa and Mukai [59] the fracture toughness of an extruded magnesium alloy is very sensitive to the crystallographic texture. In it, they used an AZ31 sample with basal poles spread towards a direction perpendicular to the extrusion axis, along which more ductile response with enhanced elongation was observed. The result of Somekawa and Mukai is in good agreement with the current results in that more ductile behavior is observed to a material direction of basal pole spread, which in our case is the RD.

In many wrought alloys, the anisotropy of failure is related to the morphology and clustering of second phase particles. Respective modelling approaches successfully capture this, e. g. [60,61]. In the current investigation, however, dispersoids are not clustered. Fracture surfaces of RD and TD tensile samples have similar appearance. Hence it is unlikely that this effect is responsible for the observed failure anisotropy.

5.3 *Advantage over full-field computations*

The evolution of deformation gradient obtained by DIC on a local fracture site was directly used to characterize the loading condition in terms of both strain and rotation imposed on the VPSC calculation. Consequently, the stress response pertaining to the fracture site was efficiently obtained without simulating the entire mechanical tests, which would require to use a full field computational framework such as finite element (FE) or fast Fourier transform (FFT) crystal plasticity simulations. In fact, the type of material failure focused in the current investigation is localized to a region corresponding to several pixels processed by the DIC technique, to which the constitutive description provided by the stand-alone VPSC code would be sufficiently representative. This approach is computationally much lighter than the case using the FE or FFT so that a more efficient evaluation of the stress response was feasible: it took less than 2 minutes to simulate the 30 separate Arcan test configurations (Table 1) by allowing multi-threading on a workstation with 2.3GHz Intel Xeon W processor.

It should be noted however that this approach cannot provide stress states from other sites than the one at which digital images are acquired, which principally restricts the method to free (visible) surfaces. In other words, as long as the DIC method is applicable, the current approach in principle can be used. Nonetheless, considering the AZ31 sheet with an initial thickness of 1.2 mm was used, the assumption of the plane-stress condition is reasonable. Moreover, the stress developed in the volume is not expected to significantly deviate from the surface stress state.

5.4 The use of mean-field crystal plasticity model

In most of the failure models belonging to the Group III, the stress state plays a key role as it provides important inputs such as triaxiality and lode angle. A plasticity model here fills this gap by providing stress evolution for a given loading history determined in terms of strain history resulting from DIC data. Often, the measured external loadcell signal is compared with the loading history calculated from FE simulations, which again relies on a chosen constitutive model. Therefore, the accuracy of plasticity model is crucial.

According to the best knowledge of the authors, for the case of magnesium alloy, Jia and Bai [14,27] have utilized the most advanced *plasticity* model to address the anisotropic fracture among the studies focusing on the Group III criteria. In the mentioned works, they chose a particular yield function (CPB) [62] that is designed to describe the SD effect observed in textured hexagonal alloys. Moreover, Jia and Bai adapted the crystallographic characteristics based on Schmid factor to distinguish the twinning and glide activities using a semianalytical Sachs model of Barnett et al. [29]. However, certain aspects of pertinent characteristics of magnesium alloys were not properly accounted for therein. For example, the evolution of anisotropic parameters in the CPB yield function were neglected despite of the pronounced differential hardening observed in magnesium alloys [15,17,21,22,26]. Moreover, the approach using a scalar Schmid factor adapted thereby cannot properly account for *multiaxial* stress conditions concurrently. To that end, some of the material parameters were calibrated in an *ad hoc* manner depending on the stress triaxiality [27] and loading condition [14]. Overall, an approach based on Schmid factor alone cannot account for multiaxial loading states together with evolution of plastic anisotropy (as evident in Figure 7b), which generally requires the Schmid tensor for each distinctive slip and twin system such as in Eq. 6.

In the current investigation a mean-field crystal plasticity (VPSC) model was adapted as the plasticity model, which successfully captured the anisotropic behavior of AZ31 sample: both SD effect and anisotropic R-value evolution. The model parameters are closely related with the micromechanical properties such as critical resolved shear stress of each deformation mode, and the Schmid tensor characterized by slip/twin plane and direction was accounted for to address the resolved shear stress determined based on multiaxial stress states of individual grains. The loading history of the fracture site obtained from DIC measurement was directly employed to VPSC model. The decoupled approach in the

current form consisting of an empirical damage indicator and a mean-field crystal plasticity model is computationally light and can effectively serve to account for various microscopic features such as texture evolution and slip/twin activities during large plastic deformation.

One of the most apparent advantage of using mean-field crystal plasticity over phenomenological plasticity model is that the constitutive parameters are more closely related with microscopic features such as crystallographic texture, twin and slip modes. Consequently, the current hybrid approach can be further explored to quantify the effects of, for instance, crystallographic texture and slip/twin activities to material fracture.

The model calibration is also quite straightforward: the initial crystallographic texture can be experimentally determined using EBSD and XRD techniques, and a fewer number of parameters were used compared to the modeling approach of Jia and Bai. Overall, 30 separate parameters (20 for semi-analytical Sachs model and 10 for eMMC criterion including transformation matrix) were calibrated in [27]. In the current approach, 16 Voce hardening parameters and 3 additional components of linear transformation matrix were calibrated. Moreover, rich information on material behavior can be extracted such as texture evolution; and the hardening parameters for individual slip/twin modes are closely related with the micromechanical features so that direct measurement of CRSS have been attempted by various microscopic techniques – see, e.g., [63] so that the well calibrated material model can be used for new material design and performance estimation.

5.5 Crack initiation point and triaxiality

So far, it has been stated here that cracks initiate at the free boundary. Although this still appears to be a true statement from the macroscopic point of view, the values of triaxiality reported in Section 4.2 raise a contradiction to that. Since the simulated values are larger than $1/3$ and the failure criterion renders valid predictions once a weight based on the local triaxiality is included in the failure model (see Figure 14b), it can be concluded that the failure process is initiated a few microns away from the edge. This appears generally feasible. If cracks initiate at the edge or a few microns away from it, it remains an open question, because

1. The fracture surfaces do not show any sign of an initiation point as against the crack propagation regime [42];
2. The approach pursued in the current investigation does not account for gradients along the sheet thickness direction. These possible constraints leading to an increase in stress triaxiality are not considered.

It is possible to impose the position of localization and subsequent cracking to a sample by applying intentional thinning to specimen prior to tests, e. g. [64,65]. Alternatively, a combined approach of testing and FE-simulations can provide the location of the maximum triaxiality to define the onset of fracture, e.g. [9,66]. The first procedure appears not to be feasible here, since machining will add mechanical twins to the material, which changes the properties of the parent material. The second is lapsed by the current approach, since the point of fracture, from which the strain history is obtained, is regarded unknown a priori.

6 Conclusion

An uncoupled ductile fracture criterion was investigated for an AZ31 magnesium alloy sheet. The criterion utilized the strain history from DIC analyses focusing on local fracture sites. A simple linear transformation was applied to account for the anisotropy in fracture behavior, which was used to quantify the accumulated damage as a scalar quantity. Although the fracture anisotropy observed in uniaxial tension results was well captured, the predictive accuracy of the damage indicator on various mixed-mode loading histories explored by Arcan tests was less accurate.

The visco-plastic self-consistent crystal plasticity provided reasonable stress responses pertaining to the local fracture in that the SD effect and the deformation-induced anisotropy were well captured. The results of VPSC simulation suggest that the damage indicator in the current form needs to additionally account for the stress triaxiality. By explicitly accounting for the triaxiality estimated by VPSC simulation, the corrected damage indicator led to consistently good predictive accuracy for various loading histories realized in three uniaxial tension and ten different mixed-mode loading histories. Although the approach is of phenomenological nature, it appears more suited to assess the fracture than instability models, since the type of strain localization assumed therein was not observed experimentally.

The analysis of the stress triaxiality at the crack initiation points of the sheet metal retrieved values lying between the values of 0.33 and 0.45, which correspond to the uniaxial (1/3) state and a marginally shifted state towards the equi-biaxial (2/3). Although the range is too small in order to formulate general dependencies between triaxiality and ductility valid for bulk material, it allows assessing the edge failure: it is likely that crack formation started away from the free surface rather than at the edge.

7 Acknowledgements

YJ acknowledges the supports from National Research Foundation of Korea (NRF-2017R1D1A1B03031052) and the Ministry of Trade, Industry, and Energy (N0002598). The authors furthermore thank Markus Ziehmer for providing the EBSD texture scans and Jacques Besson for discussions on failure anisotropy.

8 References

- [1] R. Hill, On discontinuous plastic states, with special reference to localized necking in thin sheets, *J. Mech. Phys. Solids*. 1 (1952) 19–30. doi:10.1016/0022-5096(52)90003-3.
- [2] H.W. Swift, Plastic instability under plane stress, *J. Mech. Phys. Solids*. 1 (1952) 1–18. doi:10.1016/0022-5096(52)90002-1.
- [3] Z. Marciniak, K. Kuczyński, Limit strains in the processes of stretch-forming sheet metal, *Int. J. Mech. Sci.* 9 (1967) 609–620. doi:10.1016/0020-7403(67)90066-5.
- [4] Z. Marciniak, K. Kuczyński, T. Pokora, Influence of the plastic properties of a material on the forming limit diagram for sheet metal in tension, *Int. J. Mech. Sci.* 15 (1973) 789–800. doi:10.1016/0020-7403(73)90068-4.
- [5] A.L. Gurson, Continuum Theory of Ductile Rupture by Void Nucleation and Growth: Part I—Yield Criteria and Flow Rules for Porous Ductile Media, *J. Eng. Mater. Technol.* 99 (1977) 2. doi:10.1115/1.3443401.
- [6] V. Tvergaard, Influence of void nucleation on ductile shear fracture at a free surface, *J. Mech. Phys. Solids*. 30 (1982) 399–425. doi:10.1016/0022-5096(82)90025-4.
- [7] G. Rousselier, Ductile fracture models and their potential in local approach of fracture, *Nucl. Eng. Des.* 105 (1987) 97–111. doi:10.1016/0029-5493(87)90234-2.
- [8] F.D. Fischer, O. Kolednik, G.X. Shan, F.G. Rammerstorfer, A note on calibration of ductile failure damage indicators, *Int. J. Fract.* 73 (1995) 345–357. doi:10.1007/BF00027274.
- [9] J.-Y. Lee, D. Steglich, M.-G. Lee, Fracture prediction based on a two-surface plasticity law for the anisotropic magnesium alloys AZ31 and ZE10, *Int. J. Plast.* 105 (2018) 1–23. doi:10.1016/j.ijplas.2017.10.002.
- [10] Y. Bai, T. Wierzbicki, A new model of metal plasticity and fracture with pressure and Lode dependence, *Int. J. Plast.* 24 (2008) 1071–1096. doi:10.1016/j.ijplas.2007.09.004.
- [11] Y. Bai, T. Wierzbicki, Application of extended Mohr–Coulomb criterion to ductile fracture, *Int. J. Fract.* 161 (2010) 1–20. doi:10.1007/s10704-009-9422-8.
- [12] B. Kondori, A.A. Benzerga, Fracture Strains, Damage Mechanisms and Anisotropy in a Magnesium Alloy Across a Range of Stress Triaxialities, *Exp. Mech.* 54 (2014) 493–499. doi:10.1007/s11340-013-9812-8.
- [13] B. Kondori, A.A. Benzerga, Effect of Stress Triaxiality on the Flow and Fracture of Mg Alloy AZ31, *Metall. Mater. Trans. A*. 45 (2014) 3292–3307. doi:10.1007/s11661-014-2211-7.

- [14] Y. Jia, Y. Bai, Ductile fracture prediction for metal sheets using all-strain-based anisotropic eMMC model, *Int. J. Mech. Sci.* 115–116 (2016) 516–531. doi:10.1016/j.ijmecsci.2016.07.022.
- [15] D. Steglich, Y. Jeong, M.O. Andar, T. Kuwabara, Biaxial deformation behaviour of AZ31 magnesium alloy: Crystal-plasticity-based prediction and experimental validation, *Int. J. Solids Struct.* 49 (2012) 3551–3561. doi:10.1016/j.ijsolstr.2012.06.017.
- [16] F. Kabirian, A.S. Khan, T. Gnäupel-Herlod, Visco-plastic modeling of mechanical responses and texture evolution in extruded AZ31 magnesium alloy for various loading conditions, *Int. J. Plast.* 68 (2015) 1–20. doi:10.1016/j.ijplas.2014.10.012.
- [17] W. Muhammad, M. Mohammadi, J. Kang, R.K. Mishra, K. Inal, An elasto-plastic constitutive model for evolving asymmetric/anisotropic hardening behavior of AZ31B and ZEK100 magnesium alloy sheets considering monotonic and reverse loading paths, *Int. J. Plast.* 70 (2015) 30–59. doi:10.1016/j.ijplas.2015.03.004.
- [18] R. Hill, J.W. Hutchinson, Differential Hardening in Sheet Metal Under Biaxial Loading: A Theoretical Framework, *J. Appl. Mech.* 59 (1992) S1. doi:10.1115/1.2899489.
- [19] R. Hill, S.S. Hecker, M.G. Stout, An investigation of plastic flow and differential work hardening in orthotropic brass tubes under fluid pressure and axial load, *Int. J. Solids Struct.* 31 (1994) 2999–3021. doi:10.1016/0020-7683(94)90065-5.
- [20] T. Kuwabara, S. Ikeda, K. Kuroda, Measurement and analysis of differential work hardening in cold-rolled steel sheet under biaxial tension, *J. Mater. Process. Technol.* 80–81 (1998) 517–523. doi:10.1016/S0924-0136(98)00155-1.
- [21] T. Hama, H. Takuda, Crystal plasticity finite-element simulation of work-hardening behavior in a magnesium alloy sheet under biaxial tension, *Comput. Mater. Sci.* 51 (2012) 156–164. doi:10.1016/j.commatsci.2011.07.026.
- [22] M.N. Mekkonen, D. Steglich, J. Bohlen, D. Letzig, J. Mosler, Mechanical characterization and constitutive modeling of Mg alloy sheets, *Mater. Sci. Eng. A.* 540 (2012) 174–186. doi:10.1016/j.msea.2012.01.122.
- [23] D. Ghaffari Tari, M.J. Worswick, U. Ali, M.A. Gharghouri, Mechanical response of AZ31B magnesium alloy: Experimental characterization and material modeling considering proportional loading at room temperature, *Int. J. Plast.* 55 (2014) 247–267. doi:10.1016/j.ijplas.2013.10.006.
- [24] O. Cazacu, B. Plunkett, F. Barlat, Orthotropic yield criterion for hexagonal closed packed metals, *Int. J. Plast.* 22 (2006) 1171–1194. doi:10.1016/j.ijplas.2005.06.001.
- [25] O. CAZACU, F. BARLAT, A criterion for description of anisotropy and yield differential effects in pressure-insensitive metals, *Int. J. Plast.* 20 (2004) 2027–2045.

- doi:10.1016/j.ijplas.2003.11.021.
- [26] B. Plunkett, R.A. Lebensohn, O. Cazacu, F. Barlat, Anisotropic yield function of hexagonal materials taking into account texture development and anisotropic hardening, *Acta Mater.* 54 (2006) 4159–4169. doi:10.1016/j.actamat.2006.05.009.
- [27] Y. Jia, Y. Bai, Experimental study on the mechanical properties of AZ31B-H24 magnesium alloy sheets under various loading conditions, *Int. J. Fract.* 197 (2016) 25–48. doi:10.1007/s10704-015-0057-7.
- [28] K. Inal, R.K. Mishra, O. Cazacu, Forming simulation of aluminum sheets using an anisotropic yield function coupled with crystal plasticity theory, *Int. J. Solids Struct.* 47 (2010) 2223–2233. doi:10.1016/j.ijsolstr.2010.04.017.
- [29] M.R. Barnett, Z. Keshavarz, X. Ma, A semianalytical Sachs model for the flow stress of a magnesium alloy, *Metall. Mater. Trans. A.* 37 (2006) 2283–2293. doi:10.1007/BF02586147.
- [30] M. Luo, M. Dunand, D. Mohr, Experiments and modeling of anisotropic aluminum extrusions under multi-axial loading – Part II: Ductile fracture, *Int. J. Plast.* 32–33 (2012) 36–58. doi:10.1016/j.ijplas.2011.11.001.
- [31] Y. Lou, J.W. Yoon, Anisotropic ductile fracture criterion based on linear transformation, *Int. J. Plast.* 93 (2017) 3–25. doi:10.1016/j.ijplas.2017.04.008.
- [32] C. John Neil, S.R. Agnew, Crystal plasticity-based forming limit prediction for non-cubic metals: Application to Mg alloy AZ31B, *Int. J. Plast.* 25 (2009) 379–398. doi:10.1016/j.ijplas.2008.05.003.
- [33] H. Wang, P.D. Wu, K.P. Boyle, K.W. Neale, On crystal plasticity formability analysis for magnesium alloy sheets, *Int. J. Solids Struct.* 48 (2011) 1000–1010. doi:10.1016/j.ijsolstr.2010.12.004.
- [34] D. Steglich, Y. Jeong, Texture-based forming limit prediction for Mg sheet alloys ZE10 and AZ31, *Int. J. Mech. Sci.* 117 (2016) 102–114. doi:10.1016/j.ijmecsci.2016.08.013.
- [35] R.A. Lebensohn, C.N. Tomé, A study of the stress state associated with twin nucleation and propagation in anisotropic materials, *Philos. Mag. A Phys. Condens. Matter, Struct. Defects Mech. Prop.* (1993). doi:10.1080/01418619308207151.
- [36] H. Wang, P.D. Wu, C.N. Tomé, Y. Huang, A finite strain elastic-viscoplastic self-consistent model for polycrystalline materials, *J. Mech. Phys. Solids.* 58 (2010) 594–612. doi:10.1016/j.jmps.2010.01.004.
- [37] S. AGNEW, D. BROWN, C. TOME, Validating a polycrystal model for the elastoplastic response of magnesium alloy AZ31 using in situ neutron diffraction, *Acta Mater.* 54 (2006) 4841–4852. doi:10.1016/j.actamat.2006.06.020.

- [38] C.N. Tomé, P.J. Maudlin, R.A. Lebensohn, G.C. Kaschner, Mechanical response of zirconium - I. Derivation of a polycrystal constitutive law and finite element analysis, *Acta Mater.* 49 (2001) 3085–3096. doi:10.1016/S1359-6454(01)00190-2.
- [39] R. A. Lebensohn, N-site modeling of a 3D viscoplastic polycrystal using Fast Fourier Transform, *Acta Mater.* 49 (2001) 2723–2737. doi:10.1016/S1359-6454(01)00172-0.
- [40] R.A. Lebensohn, C.N. Tomé, P.J. Maudlin, A selfconsistent formulation for the prediction of the anisotropic behavior of viscoplastic polycrystals with voids, *J. Mech. Phys. Solids.* 52 (2004) 249–278. doi:10.1016/S0022-5096(03)00114-5.
- [41] J. Park, H. Lee, J.J. Kim, O.D. Kwon, Newly developed E-form Mg in POSCO, in: 10th Int. Conf. Magnes. Alloy. Their Appl., 2015.
- [42] D. Steglich, Mixed-Mode Deformation and Failure of a Magnesium Sheet Quantified using a Modified Arcan Fixture, *Exp. Mech.* 60 (2020) 109–118. doi:10.1007/s11340-019-00542-y.
- [43] A. Savitzky, M.J.E. Golay, Smoothing and Differentiation of Data by Simplified Least Squares Procedures., *Anal. Chem.* 36 (1964) 1627–1639. doi:10.1021/ac60214a047.
- [44] E. Jones, T. Oliphant, P. Peterson, SciPy: Open source scientific tools for Python, (2001).
- [45] R.A. Lebensohn, C.N. Tomé, A self-consistent anisotropic approach for the simulation of plastic deformation and texture development of polycrystals: Application to zirconium alloys, *Acta Metall. Mater.* 41 (1993) 2611–2624. doi:10.1016/0956-7151(93)90130-K.
- [46] T. Mura, *Micromechanics of defects in solids*, Springer Science & Business Media, 2013.
- [47] C. Tome, G.R. Canova, U.F. Kocks, N. Christodoulou, J.J. Jonas, The relation between macroscopic and microscopic strain hardening in F.C.C. polycrystals, *Acta Metall.* 32 (1984) 1637–1653. doi:10.1016/0001-6160(84)90222-0.
- [48] J.D. Eshelby, The determination of the elastic field of an ellipsoidal inclusion, and related problems, *Proc. R. Soc. London. Ser. A. Math. Phys. Sci.* 241 (1957) 376–396.
- [49] A. Molinari, G.R. Canova, S. Ahzi, A self consistent approach of the large deformation polycrystal viscoplasticity, *Acta Metall.* 35 (1987) 2983–2994. doi:10.1016/0001-6160(87)90297-5.
- [50] A.P. Karafillis, M.C. Boyce, A general anisotropic yield criterion using bounds and a transformation weighting tensor, *J. Mech. Phys. Solids.* (1993). doi:10.1016/0022-5096(93)90073-O.
- [51] F. Barlat, H. Aretz, J.W. Yoon, M.E. Karabin, J.C. Brem, R.E. Dick, Linear transformation-based anisotropic yield functions, *Int. J. Plast.* 21 (2005) 1009–1039.

- doi:10.1016/j.ijplas.2004.06.004.
- [52] J.A. Nelder, R. Mead, A Simplex Method for Function Minimization, *Comput. J.* 7 (1965) 308–313. doi:10.1093/comjnl/7.4.308.
- [53] Y. Jeong, C.N. Tomé, Extension of the visco-plastic self-consistent model to account for elasto-visco-plastic behavior using a perturbed visco-plastic approach, *Model. Simul. Mater. Sci. Eng.* 27 (2019) 085013. doi:10.1088/1361-651X/ab4b66.
- [54] A. Jain, S.R. Agnew, Modeling the temperature dependent effect of twinning on the behavior of magnesium alloy AZ31B sheet, *Mater. Sci. Eng. A.* 462 (2007) 29–36. doi:10.1016/j.msea.2006.03.160.
- [55] J. Kang, D.S. Wilkinson, R.K. Mishra, W. Yuan, R.S. Mishra, Effect of inhomogeneous deformation on anisotropy of AZ31 magnesium sheet, *Mater. Sci. Eng. A.* 567 (2013) 101–109. doi:10.1016/j.msea.2012.08.117.
- [56] J.W. Hancock, A.C. Mackenzie, On the mechanisms of ductile failure in high-strength steels subjected to multi-axial stress-states, *J. Mech. Phys. Solids.* 24 (1976) 147–160. doi:10.1016/0022-5096(76)90024-7.
- [57] J.R. Rice, D.M. Tracey, On the ductile enlargement of voids in triaxial stress fields*, *J. Mech. Phys. Solids.* 17 (1969) 201–217. doi:10.1016/0022-5096(69)90033-7.
- [58] F.A. McClintock, A Criterion for Ductile Fracture by the Growth of Holes, *J. Appl. Mech.* 35 (1968) 363. doi:10.1115/1.3601204.
- [59] H. Somekawa, T. Mukai, Effect of texture on fracture toughness in extruded AZ31 magnesium alloy, *Scr. Mater.* 53 (2005) 541–545. doi:10.1016/j.scriptamat.2005.04.048.
- [60] T. Pardoen, J.W. Hutchinson, Extended model for void growth and coalescence, *J. Mech. Phys. Solids.* (2000). doi:10.1016/S0022-5096(00)00019-3.
- [61] D. Steglich, W. Brocks, J. Heerens, T. Pardoen, Anisotropic ductile fracture of Al 2024 alloys, *Eng. Fract. Mech.* 75 (2008) 3692–3706. doi:10.1016/j.engfracmech.2007.04.008.
- [62] B. Plunkett, O. Cazacu, F. Barlat, Orthotropic yield criteria for description of the anisotropy in tension and compression of sheet metals, *Int. J. Plast.* 24 (2008) 847–866. doi:10.1016/j.ijplas.2007.07.013.
- [63] R. Sánchez-Martín, M.T. Pérez-Prado, J. Segurado, J. Bohlen, I. Gutiérrez-Urrutia, J. Llorca, J.M. Molina-Aldareguia, Measuring the critical resolved shear stresses in Mg alloys by instrumented nanoindentation, *Acta Mater.* 71 (2014) 283–292. doi:10.1016/j.actamat.2014.03.014.
- [64] M. Dunand, D. Mohr, Optimized butterfly specimen for the fracture testing of sheet materials under combined normal and shear loading, *Eng. Fract. Mech.* 78 (2011)

2919–2934. doi:10.1016/j.engfracmech.2011.08.008.

- [65] Q. Yin, C. Soyarslan, K. Isik, A.E. Tekkaya, A grooved in-plane torsion test for the investigation of shear fracture in sheet materials, *Int. J. Solids Struct.* 66 (2015) 121–132. doi:10.1016/j.ijsolstr.2015.03.032.
- [66] Y. Lou, L. Chen, T. Clausmeyer, A.E. Tekkaya, J.W. Yoon, Modeling of ductile fracture from shear to balanced biaxial tension for sheet metals, *Int. J. Solids Struct.* 112 (2017) 169–184. doi:10.1016/j.ijsolstr.2016.11.034.

Appendix

The Savitzky-Golay filter has been applied to reduce the noise contained in the evolution of deformation gradient tensor (hereinafter denoted as \mathbf{F}) obtained from DIC analysis. The noise present in the discretized \mathbf{F} data is reduced by fitting a batch of successive data with a polynomial. The coefficients of polynomial are determined by the least square method. For that reason, the order of polynomial (N^o) and the number of discrete data binned in a batch (N^b) may affect the degree of smoothing. A number of (N^o, N^b) pairs were tested to demonstrate the influence of various smoothing conditions on 1) the rate of deformation gradient (\dot{F}_{11} and \dot{F}_{22}); and 2) the stress responses ($\bar{\sigma}_{11}$ and $\bar{\sigma}_{22}$) resulting from VPSC simulation using the strain rate and the rotation rate derived from the smoothed \mathbf{F} as shown in Figure 16 and Figure 17, respectively. For VPSC simulation, a raw DIC data set from a uniaxial tension test along RD was utilized. Afterwards, the stress responses from VPSC were used to estimate the average triaxiality (following Eq. 17), and the results are summarized in Figure 18.

Figures 16 and 17 suggest that the order of polynomial for the range considered in the current investigation has only a marginal effect on both $\dot{\mathbf{F}}$ and $\bar{\boldsymbol{\sigma}}$ particularly when $N^b \geq 15$. The influence of N^o becomes less significant with $N^b \geq 15$ as well. Likewise, Figure 18 suggests that for each chosen order of polynomial, N^b has only a minor effect. Considering that the loading conditions investigated in the current study does not involve drastic change, the 2nd order polynomial is regarded more adequate than higher order polynomials to prevent a potential risk of data overfitting. For a chosen polynomial, the influence of N^b seems to also have only a minor influence on $\bar{\eta}$. Note that the upper abscissa in Figure 18 scales with the ratio of the number of images in each batch to the total number of images taken before fracture. Namely, below defined \hat{N} value was used to quantify how relatively large a size of batch is:

$$\hat{N} = \frac{N^b}{N^{tot}} \times 100 [\%]$$

in which N^{tot} corresponds to the total number of images taken prior to fracture. In this study, the number of images in a batch for polynomial fit is chosen such that \hat{N} amounts to 5% unless otherwise noted.

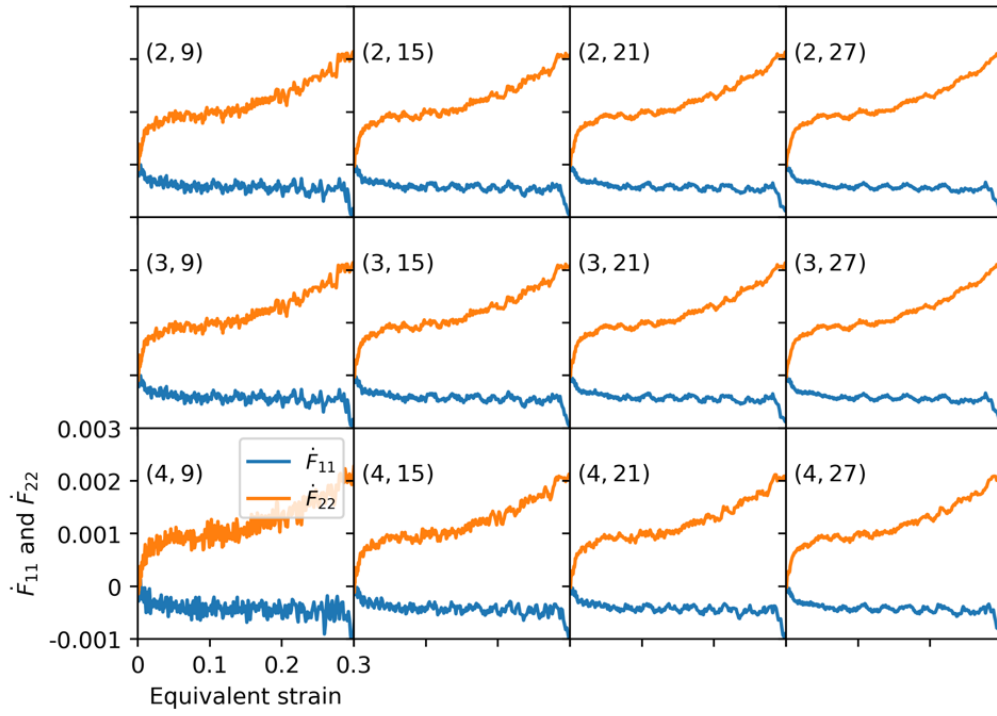


Figure 16 Rate of deformation gradient tensor (\dot{F}_{11} and \dot{F}_{22}) smoothed by Savitzky-Golay filter; Each subplot results from a set of the order of polynomial (N^o) and the number of discrete data binned (N^b), which is given in the upper left corner as in (N^o, N^b) pairs.

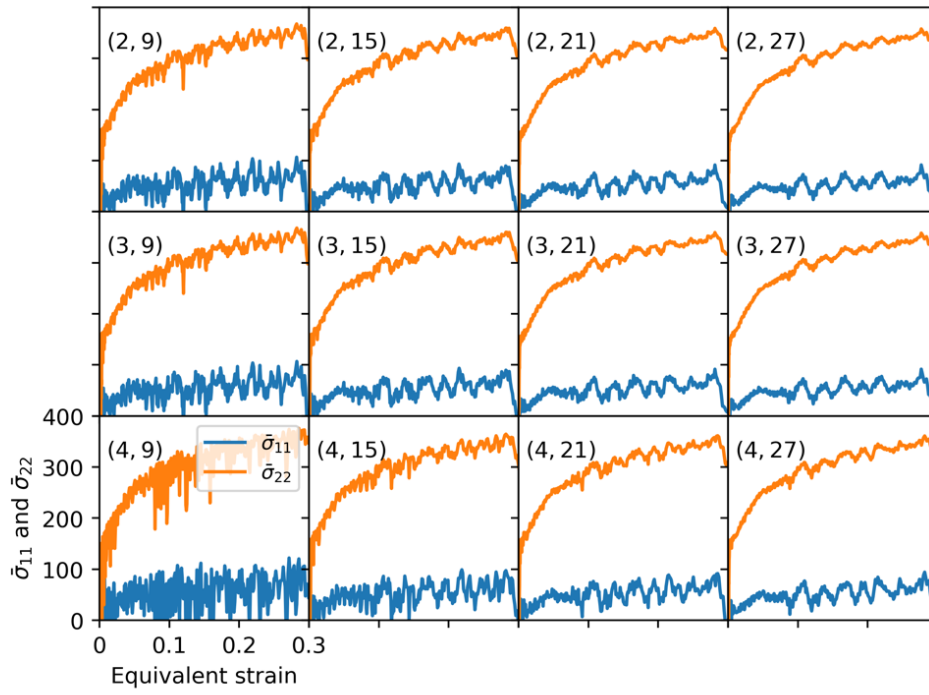


Figure 17 Stress response simulated by VPSC, which results from the Savitzky-Golay filter. The same template of Figure 16 was used.

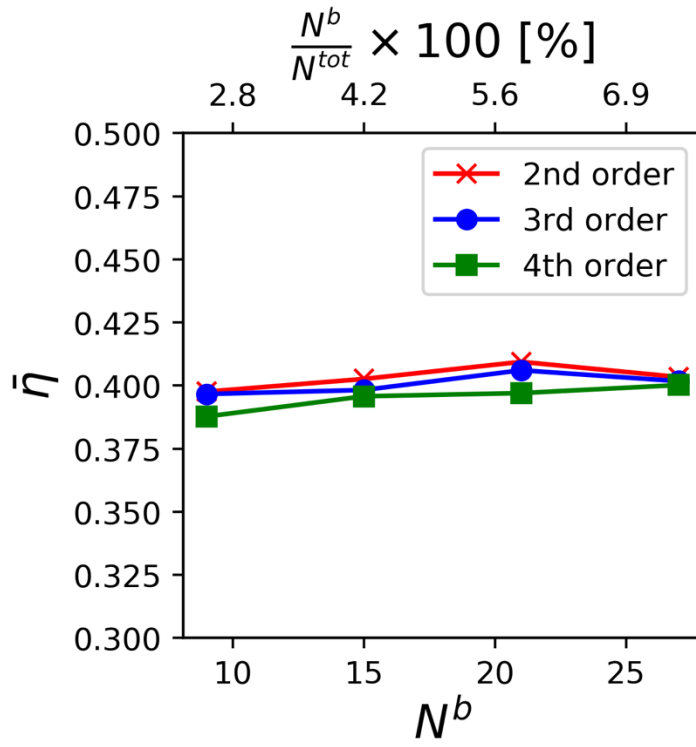


Figure 18 Averaged triaxiality $\bar{\eta}$ resulting from various (N^o, N^b) conditions assumed in the Savitzky-Golay filter.